



A Global Magnetohydrodynamic Simulation Study of Ultra-low-frequency Wave Activity in the Inner Magnetosphere: Corotating Interaction Region + Alfvénic Fluctuations

P. R. Jauer^{1,2} , C. Wang¹, V. M. Souza² , M. V. Alves², L. R. Alves², M. B. Pádua², J. P. Marchezi², Da L. A. Silva^{1,2}, Z. Liu¹, H. Li¹ , L. E. A. Vieira², A. Dal Lago², W. D. Gonzalez^{1,2}, E. Echer², C. Medeiros² , J. E. R. Costa², and C. M. Denardini²

¹ State Key Laboratory of Space Weather of National Space Science Center, Chinese Academy of Sciences, CAS, Beijing, People's Republic of China

pauloricardojauer@gmail.com

² National Institute for Space Research—INPE, São José dos Campos, SP, Brazil

Received 2019 May 7; revised 2019 September 30; accepted 2019 October 11; published 2019 November 20

Abstract

Using global magnetohydrodynamic (MHD) simulations, we investigate the role played by a complex solar structure composed of a corotating interaction region (CIR) followed by solar wind Alfvénic fluctuations on the magnetosphere's nightside, equatorial electric field oscillations in the ultra-low-frequency range. A series of numerical experiments are performed employing synthetic solar wind inputs resembling those of a real CIR + Alfvénic fluctuation event that reached Earth's magnetosphere on 2003 April 20. The following is found: (i) Radial electric field component fluctuations are excited via magnetopause boundary motions driven either by solar wind density variations characteristic of CIRs or by solar wind Alfvénic fluctuations with a given oscillation period. (ii) Azimuthal electric field component fluctuations nearer to Earth, that is, at radial distances R less than about $5R_E$ ($R_E = 1$ Earth radius), are apparently not related to either of the two types of sinusoidal solar wind Alfvénic fluctuations used in this study featuring monochromatic frequencies of 0.833 mHz (20-minute period) and 1.666 mHz (10-minute period). Instead, these innermost azimuthal component fluctuations show enhanced activity when inner magnetosphere convection increases as a result of a southward turning of the interplanetary magnetic field component B_z . (iii) Lastly, outermost ($R \gtrsim 7R_E$) azimuthal electric field oscillations weakly respond to monochromatic solar wind Alfvénic fluctuations by showing power spectral density peaks at both driving frequencies, but only near the flanks of the magnetopause, thus suggesting that such oscillations are being excited also owing to magnetopause boundary motions driven by solar wind Alfvénic fluctuations.

Unified Astronomy Thesaurus concepts: [Magnetohydrodynamical simulations \(1966\)](#); [Solar-terrestrial interactions \(1473\)](#); [Alfvén waves \(23\)](#)

1. Introduction

The physical processes that control the interaction between the Sun–Earth system are connected by different plasma components that can interact mutually and trigger a series of effects that can be observed at Earth's magnetosphere. The magnetosphere cavity is a region where the geomagnetic field plays a major role in a series of processes such as dayside magnetic field reconnection at the magnetopause boundary (Dungey 1961; Vasylunas 1975; Souza et al. 2017a), as well as in the injection of tens to hundreds of keV energy particles at Earth's magnetotail via geomagnetic substorms and their subsequent acceleration to MeV energies through the so-called wave–particle interactions (see, e.g., Claudepierre et al. 2008; Souza et al. 2017b, and references therein).

Due to the magnetosphere's inherently large dimensions, it becomes problematic to address the aforementioned processes simultaneously, particularly from an observational point of view. That is where the global ideal magnetohydrodynamic (MHD) simulations, usually coupled with inner magnetosphere models, come in (e.g., Lyon et al. 2004; Tóth et al. 2012; Claudepierre et al. 2016). Global MHD simulations have been extensively used as an important tool in space plasma physics to understand the large-scale interaction between the disturbed solar wind and Earth's magnetosphere. Specifically, they have been employed to address the generation of low-frequency waves (in a few to tens of mHz range) like ultra-low-frequency (ULF) waves in the inner magnetosphere and their possible effect on particle energization and transport in the (usually) two

donut-shaped, mainly field-aligned structures encircling Earth known as the radiation belts (e.g., Claudepierre et al. 2008, 2010; McGregor et al. 2014; Ellington et al. 2016; Alves et al. 2017; Komar et al. 2017; Souza et al. 2017b; Da Silva et al. 2019). Claudepierre et al. (2008) used the Lyon–Fedder–Mobarry (LFM; Lyon et al. 2004) global MHD code to analyze the response of Earth's magnetosphere in terms of the production of ULF waves during periods when Earth is subject to idealized high-speed solar wind streams (HSSs). They found that magnetopause motions in the flank regions consistent with those driven by the Kelvin–Helmholtz (KH) instability were driving ULF waves in the inner magnetosphere. They further showed that KH waves could effectively interact with a few hundred keV energy, equatorially mirroring electrons in the outer radiation belts. A study using the Space Weather Modeling Framework/Block-Adaptive-Tree Solarwind Roe-type Upwind-Scheme (SWMF/BATS-R-US; Tóth et al. 2012) global MHD code showed that the magnetic wave power integrated in the ULF wave (0.5–16.6 mHz) range in the equatorial, nightside magnetosphere can be increased by 100% or more when the magnetosphere is being driven by interplanetary magnetic field (IMF) B_z monochromatic fluctuations with slightly negative, as opposed to positive, average values (Souza et al. 2017b). Such enhanced ULF wave power, along with the presence of increased whistler mode chorus waves activity, was argued to play the major role in the replenishment of the relativistic ($\gtrsim 1$ MeV) outer belt electron fluxes during the period when Earth's magnetosphere was under the influence of an HSS (Souza et al. 2017b). McGregor et al. (2014) used the LFM



code to show that adding coupled magnetic and velocity field fluctuations of Alfvénic nature on top of simulated solar wind plasma parameters for an HSS resulted in an enhancement of ULF wave power on the dayside magnetosphere and along the flanks. We note, however, that the initially imposed Alfvénic fluctuations were not directly responsible for the driving of ULF waves in the McGregor et al. (2014) simulations. Instead, they enhanced the flank KH instability and generated dynamic pressure fluctuations, which themselves drove the ULF oscillations on the dayside and along the flanks.

Since both HSS and solar wind Alfvénic fluctuations have been shown to influence the inner magnetosphere dynamics, this work makes use of global MHD simulations to analyze a complex interplanetary structure, namely, a corotating interaction region (CIR), which precedes an HSS, followed by solar wind Alfvénic fluctuations. Specifically, a series of controlled SWMF/BATS-R-US numerical experiments are employed to understand the impact that such a complex interplanetary structure might have on the ULF wave range-integrated convection electric field fluctuations in the equatorial, nightside magnetosphere. The electric field fluctuations, particularly those that lie along the drift path of the inner magnetosphere electrons, are known to either energize outer radiation belt electrons up to a few MeV energies (e.g., Elkington 2006; Souza et al. 2017b, and references therein) or promote their outward diffusion, thus contributing to the removal of electrons from the radiation belts (see, e.g., Alves et al. 2017; Da Silva et al. 2019). That is why only the electric field variations are analyzed here. We emphasize, however, that the wave-particle interaction aspect is an issue to be addressed in a future work.

This manuscript is organized as follows. Section 2 shows the in situ spacecraft data used to motivate some of the analysis performed here. Section 3 describes in detail all the numerical experiments performed with the SWMF/BATS-R-US global MHD code, as well as a brief description of such a tool, and the analysis methods. Section 4 presents the results, Section 5 provides discussions, and Section 6 gives a summary and conclusions.

2. Data Set

The solar wind data measured at the Lagrangian L1 location used in this study were obtained by the instruments on board the *Advanced Composition Explorer* (ACE) spacecraft (Stone et al. 1998). Specifically, the magnetic field and the plasma data at 64 s time resolution were acquired by the Magnetic Field Detector and the Solar Wind Electron, Proton, and Alpha Monitor instruments, respectively.

3. Methodology

3.1. Global MHD Code

The MHD approximation has been widely used to describe space plasmas, especially in the context of the magnetospheric environment (Ogino et al. 1992; Lyon et al. 2004; Tóth et al. 2012; Wang et al. 2013). In general, MHD simulation models are built considering a single conductive fluid satisfying the conservation laws and Maxwell’s equations. In spite of it being successfully used to address the large-scale aspect of the solar wind-magnetosphere interaction, the ideal MHD simplification is not proper to describe the variety of particle species with different energy levels in the inner magnetosphere, like those composing the ring current, which goes from tens to hundreds

of keV, as well as more energetic particles in the multi-MeV range populating Earth’s radiation belts. To circumvent this issue, some authors proposed to couple kinetic models to single-fluid models in a self-consistent fashion (De Zeeuw et al. 2004). This approach is applied to the SWMF/BATS-R-US (Tóth et al. 2012; Gombosi et al. 2001, and references therein) global MHD code, developed at the University of Michigan in the Center for Space Environment Modeling (CSEM). The SWMF allows us to couple 12 components that model physical processes taking place at the solar surface and all the way up to Earth’s upper atmosphere (Tóth et al. 2012).

To better capture the inner magnetosphere dynamics during the complex interplanetary event being analyzed here, we chose to use three components of the SWMF/BATS-R-US, namely, global magnetosphere (GM; Powell et al. 1999), inner magnetosphere (IM; Toffoletto et al. 2003), and the ionosphere electrodynamics module (Ridley et al. 2004) in a configuration similar to that presented in Alves et al. (2017). The main difference in this work is that we employed a $(1/4)R_E$ uniform grid spacing in a region with dimensions $-32 < x < 12$, $-12 < y < 12$, and $-7 < z < 7$, where the spatial coordinates are in the Geocentric Solar Magnetosphere (GSM) system and in units of R_E . This domain includes part of the equatorial nightside region where we are going to focus our attention. SWMF/BATS-R-US’s Cartesian grid increases the spatial resolution by factors of two as one approaches Earth. Far downstream in the solar wind region the coarsest grid resolution used was $4R_E$. In the upstream region, however, specifically at $x > 12R_E$, a finer grid resolution of $(1/2)R_E$ has been used. The simulation domain size was $-224 < x < 32$ and $-64 < y, z < 64$, for all simulations in this study. The Pedersen conductivity was fixed at 10 siemens throughout the analyzed period. The inner boundary of SWMF/BATS-R-US is delimited by a $2.5R_E$ sphere, centered at Earth. Over this surface the uniform plasma density number and the temperature were specified at 28 cm^{-3} and $T = 25,000 \text{ K}$, respectively.

In what follows, we describe the numerical experiments used to analyze the response of the modeled Earth’s magnetosphere to the arrival of a complex interplanetary structure in terms of convection electric field fluctuations in the ULF frequency range.

3.2. Numerical Experiments

Our analysis focuses on an 18 hr long period starting at around 12:20 Universal Time (UT) on 2003 April 20, when a CIR followed by solar wind Alfvénic fluctuations reached the ACE spacecraft, which is located at the Lagrangian L1 point. Such interplanetary structure, hereafter referred to as “RCA” (which stands for “Real CIR-Alfvén”), may persist for several solar rotations. Eventually, it impinges on Earth’s magnetosphere, leading to several physical processes, such as geomagnetic storms and substorms (Tsurutani et al. 2006). Moreover, magnetic and electric field fluctuations in the ULF frequency range can be driven in the magnetosphere’s nightside sector, playing an important role, for instance, in the outer radiation belt electron flux variability (e.g., Baker et al. 1997; Ozeke et al. 2014; Alves et al. 2017; Souza et al. 2017b, and references therein). A drawback one usually encounters when trying to investigate (possible) causal relations between solar wind parameters in RCAs and physical processes in the inner magnetosphere is the fact that in some cases it might be quite hard to disentangle the effects due to either one of the RCA’s

Table 1
Simulations Performed in This Work

Simulation Identifier	Simulated Period (hr)	Type of Solar Wind Input
RCA	18	Actual solar wind input (black lines in Figure 1)
SCA10	18	Averages at intervals Δt_1 to Δt_4 . $T_f = 10$ minutes
SCA20	18	Averages at intervals Δt_1 to Δt_4 . $T_f = 20$ minutes
SC	11	Averages at intervals Δt_1 to Δt_3 .
SA10	7	Averages at intervals Δt_3 to Δt_4 . $T_f = 10$ minutes
SA20	7	Averages at intervals Δt_3 to Δt_4 . $T_f = 20$ minutes

Note. T_f is the fluctuation period used to mimic Alfvénic fluctuations in the synthetic solar wind input. Refer to Table 2 for definition of Δt values.

components, namely, the CIR and the solar wind Alfvénic fluctuations. However, in a controlled, global MHD simulation environment one can investigate the effects of each component separately, as well as of the RCA event as a whole. Here, we are particularly interested in the generation of electromagnetic field fluctuations in the ULF frequency range on the nightside, equatorial magnetosphere when Earth’s magnetic environment was under the influence of the 2003 April RCA event. In Table 1, we show the list of the numerical experiments performed. In the experiments, we separate this RCA into simpler parts, namely, a pure CIR-like component and a pure solar wind Alfvénic fluctuation component, with the latter having a fluctuation period of either 10 minutes or 20 minutes. It is noticed that all simulations were initialized using a feature of SWMF/BATS-R-US whereby the convergence of the numerical solution is sped up so that a quasi-steady state can be achieved before SWMF is fed with the solar wind input data (Tóth et al. 2012; Ellington et al. 2016).

In the following subsections, we provide details on how each numerical experiment in Table 1 was built and how the SWMF/BATS-R-US’s convection electric field ($\mathbf{E} = -\mathbf{V} \times \mathbf{B}$) outputs have been analyzed so we can infer which RCA component, or combinations thereof, most contributed to the generation of ULF wave activity in the inner magnetosphere, as far as MHD simulations are concerned.

3.2.1. RCA Event Description

Figure 1 shows the solar wind parameters measured by the ACE satellite during an 18 hr long period starting at 12:00 UT on 2003 April 20. From top to bottom we have (a) proton solar wind density, (b) V_y and (c) V_z solar wind velocity components, and IMF (d) B_y and (e) B_z components. The solar wind temperature throughout the period ranged between 6.54×10^4 K and 1.85×10^5 K (not shown). Likewise, the IMF B_x ranged from 0.1 to 4.1 nT, and the solar wind V_x varied between -510 and -537 km s $^{-1}$. Notice that ACE solar wind data presented in Figure 1 have been time-shifted (at https://ccmc.gsfc.nasa.gov/requests/GetInput/get_ace_L2.php) to account for solar wind propagation from ACE’s L1 location to $x_{\text{GSM}} = 32R_E$, which matches the boundary location where solar wind input is fed into SWMF/BATS-R-US.

The RCA’s CIR component is essentially identified by two abrupt changes in the solar wind density (black line) in

Figure 1(a), wherein the first one occurs at around 13:00 UT and the second one at $\sim 22:30$ UT. During this ~ 9.5 hr long period, the density plateaued around 15 cm $^{-3}$, most likely compressing the magnetosphere appreciably. After around 22:30 UT, the density decreased back to nominal values of ~ 5 cm $^{-3}$, which persisted for the remainder of the analyzed period. The initial 11 hr period going from 12:00 UT to 23:00 UT on April 20 was termed as “CIR,” and it is indicated in Figure 1 by a corresponding black, double-arrow line. It is pointed out that during such a period ground-based magnetometers sweeping the $\sim 14:00$ – $00:00$ magnetic local time (MLT) sector measured an appreciable intensification in the ULF wave activity across a broad range of L shells that initiated at $\sim 12:00$ UT, as marked by the leftmost vertical dashed line in Figure 7 in Appendix A.

Around 23:00 UT onward, both B_y and B_z components (Figures 1(d), (e)) became mostly negative, reaching ~ -5 nT and maintaining this value for about 1 hr, after which a series of irregular fluctuations initiated, not only in both magnetic field components but in the two solar wind velocity components as well (Figures 1(b), (c)). The 7 hr long period starting at 23:00 UT marks the start of a period characterized mainly by Alfvénic fluctuations in the solar wind data, and it was termed as “ALF” in Figure 1. By “Alfvénic” we mean that fluctuations in the corresponding magnetic field and velocity field components show either a clear correlation or anticorrelation, since for an Alfvén wave $\delta V_{\text{measured}} \propto \delta V_A \propto \delta B$, where δ means a variation of the field component relative to some mean value and V_A is some component of the Alfvén velocity. In fact, Alfvénic fluctuations persisted for a longer time after 06:00 UT on April 21 (see, e.g., Prestes et al. 2017). We focused only on these initial 7 hr, mainly because simulating longer intervals would require an appreciable computational power, and also we wanted to focus on the transition from CIR to Alfvénic fluctuations. When looking at ground-based magnetometer data in Figure 7 in Appendix A, one can see that after 23:00 UT ULF wave activity is further increased at outer L shells and mostly in the post-midnight and dawn sectors, coinciding with the period of southward IMF B_z and the start of the Alfvénic fluctuations. We emphasize, however, that the ground-based magnetometer data presented in this work were used solely to verify the existence of ULF wave activity at the region (and period) of interest, and therefore it is not the purpose of the present study to compare MHD simulation outputs with ground-based observational data.

3.2.2. Synthetic Profiles Setup

We now turn to a description of the simulations we performed in this study, as shown in Table 1. The first simulation (top row in Table 1) used actual solar wind data from ACE, i.e., the one from the RCA event shown as black lines in Figure 1. The simulated period was 18 hr, with Earth’s dipole tilt angle being updated as the simulation progressed. This simulation was also termed as “RCA,” with “R” standing for “real” and “CA” referring to CIR and Alfvénic fluctuations. This simulation is regarded as our reference simulation, against which the outputs of all other numerical experiments will be compared. All other simulations presented in Table 1 had no dipole tilt, and synthetic solar wind input parameters have been used with the corresponding simulation identifier starting with an “S,” which stands for “synthetic.” We considered basically three types of numerical experiments: (i) a CIR followed by

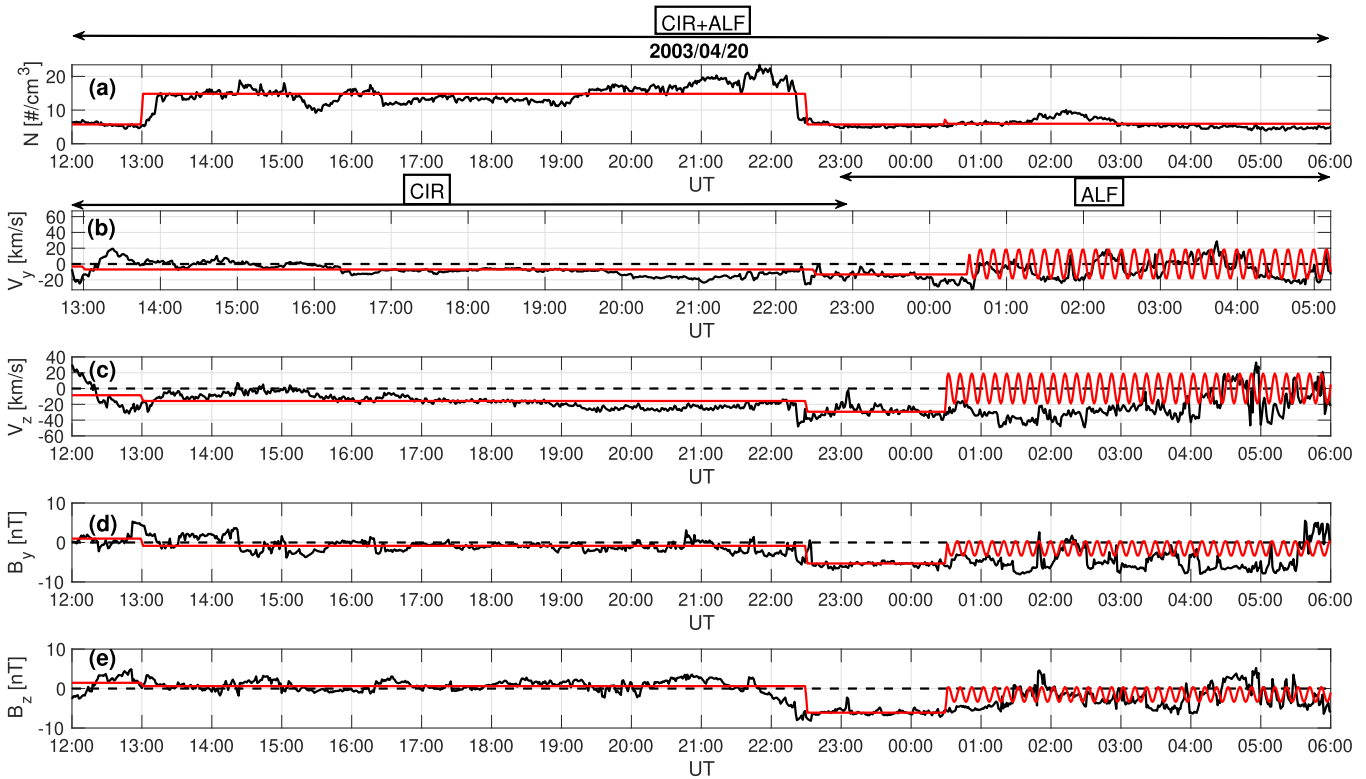


Figure 1. Real (black lines) and synthetic (red lines) solar wind data for an 18 hr period starting at 12:00 UT 2003 April 20. Actual solar wind data were obtained by the *ACE* satellite. The synthetic profiles are used as SWMF/BATS-R-US’s input data. They were constructed by averaging solar wind parameters over four time intervals depicted in Table 2.

Table 2
Intervals Used for Averaging *ACE*’s Solar Wind Data to Generate the Synthetic Profiles

Interval	Duration (in Figure 1)	$[B_x, B_y, B_z]$ (nT)	$[V_x, V_y, V_z]$ (km s $^{-1}$)	N (cm $^{-3}$)	T ($\times 10^4$ K)
Δt_1	12:00–13:00 UT	[3.030, 1.035, 1.433]	[−537.805, −3.384, −8.630]	5.734	6.537
Δt_2	13:00–22:30 UT	[0.126, −0.885, 0.539]	[−510.367, −7.068, −16.026]	14.748	6.354
Δt_3	22:30–00:30 UT	[4.111, −5.385, −6.058]	[−503.087, −15.856, −28.877]	5.384	8.093
Δt_4	00:30–06:00 UT	[3.142, $B_y(t)$, $B_z(t)$]	[−531.263, $V_y(t)$, $V_z(t)$]	5.943	18.548

Alfvénic fluctuations (SCA), (ii) a pure CIR component (SC), and (iii) a pure solar wind Alfvénic fluctuation component (SA). For the numerical experiments containing magnetic and velocity field component fluctuations of Alfvénic nature, i.e., SCA and SA simulations, we chose to use two fluctuation periods T_f of 10 and 20 minutes following previous studies of Komar et al. (2017) and Souza et al. (2017b), respectively. Thus, the corresponding simulation identifiers in Table 1 carry these numbers, which refer to the fluctuation period used in the Alfvénic fluctuation component of the synthetic solar wind inputs.

The synthetic profiles are shown as red lines in Figure 1, and they were generated as averages of the solar wind parameters in four subintervals denoted by Δt_i , with $i = 1-4$, and described in Table 2. The reasoning for doing the averages is that we wanted the simulations with synthetic input data to maintain the overall characteristics of the actual solar wind structures. For the last subinterval Δt_4 , when there are solar wind fluctuations of Alfvénic nature, the y and z components of the IMF and proton solar wind velocity were chosen to vary in time according to an Alfvén wave of monochromatic frequency

$1/T_f$, as follows:

$$\begin{aligned}
 B_y(t) &= B_{\text{avg}} + B_o \sin(2\pi t/T_f), \\
 B_z(t) &= B_{\text{avg}} + B_o \cos(2\pi t/T_f), \\
 V_y(t) &= V_o \sin(2\pi t/T_f), \\
 V_z(t) &= V_o \cos(2\pi t/T_f),
 \end{aligned} \tag{1}$$

where $B_{\text{avg}} = -1.5$ nT is the fluctuation baseline, $B_o = 2.0$ nT the field perturbation, and $V_o = 20$ km s $^{-1}$ the velocity perturbation. It is noted that V_o nearly matches the Alfvén speed (≈ 18 km s $^{-1}$) based on the chosen magnetic field perturbation B_o and the average density (5.943 cm $^{-3}$) during Δt_4 . Since both magnetic field components were mostly negative from 23:00 UT onward, we chose the baseline of the magnetic field component fluctuations to be slightly negative. The synthetic y and z components of the velocity field and IMF shown in the rightmost part of Figures 1(b)–(d) follow Equations (1) for a fluctuation period of $T_f = 10$ minutes.

For each simulation, convection electric field fluctuations in the ULF frequency range were excited. Next, we describe the

procedure employed in all simulations to analyze such electric field fluctuations.

3.2.3. Power Spectral Density Analysis

In order to analyze the level of electromagnetic field fluctuations inside the magnetosphere, more precisely in the equatorial, nightside region, we calculated the power spectral density (PSD) of the convection electric field using outputs from all simulations identified in Table 1. The MHD model does not calculate directly the electric field \mathbf{E} , so what we do to obtain it is to perform the cross product between the local magnetic \mathbf{B} and velocity \mathbf{V} field vectors, i.e., $\mathbf{E} = \mathbf{B} \times \mathbf{V} = -\mathbf{V} \times \mathbf{B}$, throughout the simulation domain. Then, the electric field vector is rotated to the field-aligned coordinate (FAC) system wherein the fluctuations are split in the direction parallel to the local field direction (denoted by the unitary vector $\hat{\mathbf{b}}$) and the azimuthal ($\hat{\phi}$) and radial ($\hat{\mathbf{r}}$) directions. The FAC system is defined here as follows: for each point $\mathbf{p} = (x, y, z)$ of space where there is a local magnetic field vector \mathbf{B} , the parallel direction is represented by the unitary vector along the local magnetic field direction, i.e., $\hat{\mathbf{b}} = \mathbf{B}/|\mathbf{B}|$, while the azimuthal ($\hat{\phi}$) direction is given by the cross product between $\hat{\mathbf{b}}$ and the unitary position vector $\hat{\mathbf{p}} = \mathbf{p}/|\mathbf{p}|$, and the radial ($\hat{\mathbf{r}}$) direction completes the orthonormal, right-handed system, with $\hat{\mathbf{r}}$ being positive radially outward.

We focus on the electric field evaluated along the nightside sector of the modeled magnetosphere from 18:00 local time (LT) to 06:00 LT at $z_{\text{GSM}} = 0$, i.e., at the equator. At a given LT, and starting at a radial distance $R = 2.5R_E$, time series of both the azimuthal (E_ϕ) and radial (E_r) electric field components were acquired, with the size of each time series depending on the simulated period shown in the second column of Table 1. For the RCA, SCA10, and SCA20 simulations, which had a simulated period of 18 hr, each electric field component’s time series had a total of $18 \times 3600/30 = 2160$ data points, where the “30” is the chosen SWMF/BATS-R-US’s output dumping rate in seconds. With such a dumping rate and number of data points, the highest resolvable frequency was 16.667 mHz, and the frequency resolution Δf was $\Delta f = 0.0154$ mHz. For the SC and SA (either 10 or 20) simulations, the time series’ sizes were 1320 and 840 points, respectively, and the corresponding frequency resolutions were $\Delta f = 0.0253$ mHz and $\Delta f = 0.0396$ mHz. A fast Fourier transform, as done by Claudepierre et al. (2008), has been employed in each (FAC-rotated) electric field component time series, and the corresponding PSDs were obtained in units of $(\text{mV/m})^2/\text{Hz}$. In the next step the radial distance R was incremented in steps of $dR = 0.065R_E$, while maintaining the same LT, and the process was repeated until $R = 9R_E$ was reached. Next, we integrated each PSD in a specific frequency band $f \in [f_a, f_b]$ depending on the simulation. For instance, for the RCA one, where we have the presence of multiple frequencies, we integrated the PSDs in the whole frequency band, that is, between $f_a = 0.5$ and $f_b = 16.667$ mHz, as done by Souza et al. (2017b). The same procedure has been applied to the SC simulation, since for this one there was no initially imposed solar wind fluctuation with a given monochromatic frequency, as was the case for the remaining synthetic simulations, namely, SCA10, SCA20, SA10, and SA20. For these four cases, unless otherwise stated, the PSDs have been integrated in a narrow frequency band centered on the driving

frequency f_o , i.e., for both SCA10 and SA10, which had a driving frequency $f_o = 1.66$ mHz ($T_f = 10$ minutes), the lower and upper bounds were, respectively, $f_a = f_o - 0.25$ mHz and $f_b = f_o + 0.25$ mHz, and likewise for the SCA20 and SA20 simulations, whose driving frequency was $f_o = 0.83$ mHz ($T_f = 20$ minutes), yielding the integrated power spectral density (IPSD):

$$\text{IPSD}_{\phi,r} = \int_{f_a}^{f_b} \text{PSD}_{E_\phi, E_r} df, \text{ units of } (\text{mV/m})^2. \quad (2)$$

In this way we have a set of representative values of the modeled electric field wave power in the Pc4–5 frequency range for a given LT and a given radial distance R . Finally, we discretized the nightside, equatorial region into 50 equally sized LT bins starting, as mentioned above, at 18:00 LT and ending at 06:00 LT. Then a map of IPSD values as a function of radial distance and LT was obtained for each simulation in Table 1, and they will be presented and discussed in the next section.

4. Results

The simulation performance was validated following the procedure proposed by Welling & Ridley (2010), whereby in situ geosynchronous magnetic field component data from the *GOES-12* satellite have been directly compared with SWMF/BATS-R-US’s magnetic field components, from the RCA event simulation, acquired along *GOES-12*’s orbit track. More details on the quantitative comparison can be found in Figure 8 in Appendix B. The validation of our simulation provided some reliability to the numerical results that will be discussed next.

In what follows, we divide the IPSD analysis by considering two cases: first, we integrate the electric field components’ Fourier spectrum for the whole simulated period, as discussed in Section 3.2.3, and second, we split each time series into 2 hr long “chunks” and then perform the Fourier spectrum’s integration in each of these pieces, so one can have a feeling on how the IPSD values change as a function of time.

4.1. IPSDs Using the Whole Time Series

Figure 2 shows the color-coded IPSD values in the equatorial, nightside region for simulations RCA (panels (a) and (e)), SCA10 (panels (b) and (f)), SC (panels (c) and (g)), and SA10 (panels (d) and (h)). The IPSDs for the azimuthal (radial) component of the convection electric field are shown in the top (bottom) row of Figure 2. Notice that the frequency band in which the E_ϕ ’s and E_r ’s power spectral densities have been integrated is shown on the left-hand side of each color bar in Figure 2. For both SCA10 and SA10 simulations the IPSDs were obtained in a narrow frequency band centered on the driving frequency $f_o = 1.66$ mHz, as mentioned in Section 3.2.3. IPSDs from the synthetic simulations are meant to help in the understanding of each RCA’s event component contribution in the generation of electric field fluctuations in the ULF range.

We start off by analyzing the level of electric field fluctuations, as measured by the IPSD parameter, in the RCA simulation, which used actual solar wind data from the 2003 April RCA event. When looking at IPSDs for the RCA simulation (Figures 2(a), (e)), the azimuthal electric field (E_ϕ) component is mainly excited in the 23:00–03:00 LT range and up to radial distances less than about $6R_E$. As for the radial electric field (E_r) component, it is mainly excited in the flank

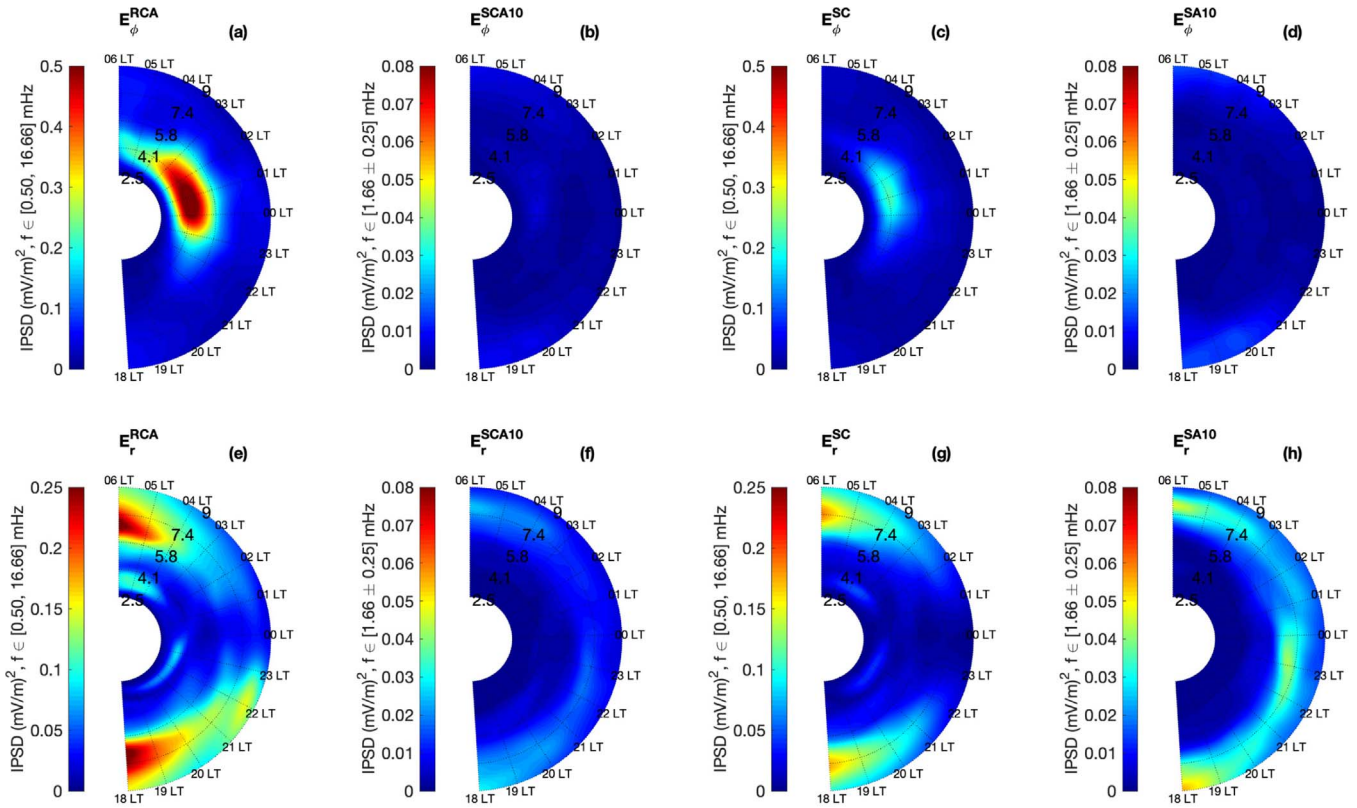


Figure 2. IPSDs of the azimuthal E_ϕ (top row) and radial E_r (bottom row) modes in the equatorial, nightside magnetosphere for simulations presented in Table 1. The frequency band used for integrating the power spectral densities is shown on the left-hand side of each color bar.

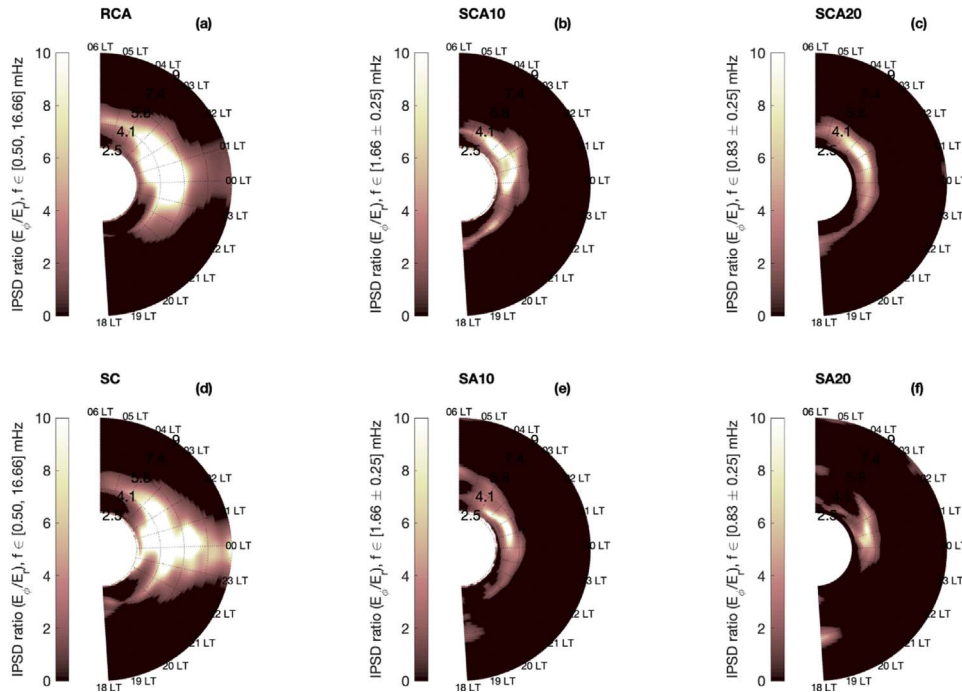


Figure 3. Ratios of IPSDs associated with the azimuthal IPSD_ϕ and radial IPSD_r electric field components for all simulations presented in Table 1. Dark regions in each panel indicate where $\text{IPSD}_r > \text{IPSD}_\phi$. The frequency band used for integrating the power spectral densities is shown on the left-hand side of each color bar.

regions of the modeled magnetosphere, i.e., from 05:00 to 06:00 LT and from 18:00 to 19:00 LT. Such activity is mostly associated with inward and outward magnetopause boundary motions owing to the interaction of the RCA's CIR component with Earth's magnetosphere. It is worthwhile mentioning that

when compared to the radial electric field component, the azimuthal (E_ϕ) component showed larger IPSD_ϕ values, i.e., between one and two orders of magnitude, in a region roughly centered at 00:00 LT spanning about 4 hr in local time and at radial distances less than about $6R_E$, as shown in Figure 3(a),

which presents $\text{IPSD}_\phi/\text{IPSD}_r$ ratios of all simulations in Table 1. The radial component, however, was higher than the azimuthal one (look at dark regions in Figure 3(a)) mostly in the flank regions, but only by, at most, a factor less than 8.

When analyzing the IPSD results for the simulation of the RCA event with synthetic solar wind parameters and with a 10-minute-period Alfvénic fluctuation (SCA10, Figures 2(b), (f)), one can see that the radial (E_r) component shows signs of fluctuations having essentially the same frequency of the driving frequency $f_o = 1.66$ mHz. Since the PSD integration has been performed in a narrower frequency band, the corresponding IPSD has a lower intensity when compared to those from the RCA event (see color bars in Figures 2(a), (e)). It is seen that radial component fluctuations at the driving frequency are excited mainly along the flanks at radial distances larger than about $7R_E$, which again reinforces the claim made above that magnetopause boundary motions are the main contributor for exciting such radial electric field component oscillations. As for the azimuthal (E_ϕ) component fluctuations, however, one could say in a first glance that they do not seem to respond to the imposed driving frequency, at least not in the same way that the radial component does. When investigating the frequencies present in the E_ϕ 's time series via Fourier analysis, though, one can clearly distinguish the presence of the driving frequency, but only at larger radial distances ($R > 7R_E$) and along the flank regions (LT = 06), as shown in Figure 4(a) for the SCA10 simulation. The narrow band centered on the driving frequency $f_o = 1.66$ mHz is presented in Figure 4 as a pair of vertical black dashed lines, and the driving frequency itself is marked as a vertical magenta dashed line. The spectral power at the driving frequency shows a readily discernible peak that is about one order of magnitude higher than those at the surrounding frequencies. We note, however, that at lower radial distances (red lines in Figures 4(a), (c)) and also for local times near and at LT = 00, the E_ϕ component does not seem to respond to the driving frequency in the same way that it does at larger radial distances. Rather, it shows the contribution of “higher” (>4 mHz) frequencies that are associated with velocity field component fluctuations (not shown) driven by the Rice Convection Model (RCM; Toffoletto et al. 2003; De Zeeuw et al. 2004). In fact, such “higher” frequencies are the ones that contribute most to the total (that is, integrated in the whole 0.5–16.66 mHz band) IPSD at lower radial distances ($R \sim 4R_E$). The insets in Figure 4 show exactly this behavior. They present the integration of the corresponding PSDs, as a function of radial distance, in three frequency bands, namely, from 0.5 to 4 mHz (magenta curve), from 4 to 16.66 mHz (green curve), and for the whole band (black curve). At midnight local time, i.e., at LT = 00, E_ϕ 's fluctuations at “higher” frequencies dominate the total IPSD irrespective of radial distance. Notice that the maximum IPSD_ϕ value of ~ 0.36 (mV/m)² is reached around $R = 4R_E$ and is similar to those found in Figure 2(a) for the RCA simulation (~ 0.56 (mV/m)²), thus indicating that such “higher” frequencies are contributing more to IPSD_ϕ values in the RCA simulation. The “lower” (<4 mHz) frequencies, which include the driving frequencies used in this study, do contribute more to the total IPSD_ϕ (black curve) at larger radial distances and at local times near the flanks of the magnetopause boundary (Figure 4(a)). The same argument holds for the radial

E_r component (see Figures 4(b), (d)), although the total IPSD for this component is a factor of ~ 5 times larger than that for E_ϕ 's total IPSD at the same local time, that is, at LT = 06.

Now we analyze the IPSDs for each one of the RCA's event components, i.e., the CIR, whose simulation identifier is “SC,” and solar wind Alfvénic fluctuations with a period of 10 minutes, whose simulation identifier is SA10. The former had its Fourier spectra integrated in the whole (0.5–16.66 mHz) band, while the latter over the narrow 1.66 ± 0.25 mHz band. Let us first look at the IPSD of the azimuthal component (top row in Figure 2) for the RCA, SC, and SA10 simulations. The enhanced IPSD_ϕ values for the SC simulation bear some similarities to those from the RCA one with respect to the spatial structure. A closer look at the SC simulation's Fourier spectra for the E_ϕ component, as shown in Figures 4(e), (g), reveals that the enhanced IPSD_ϕ values nearer to Earth ($R \sim 4R_E$) are dominated by the “higher” (>4 mHz) frequency components, which do *not* include the driving frequencies analyzed here. Indeed, we did expect that the SC simulation would not necessarily provide electric field fluctuations matching either of the two driving frequencies used in this study, since neither of them has been initially imposed as an input boundary condition for the SC simulation, which did not feature Alfvénic fluctuations. In fact, there is no discernible sign of the driving frequency $f_o = 1.66$ mHz (nor $f_o = 0.83$ mHz) for E_ϕ 's PSD at farther distances near the modeled magnetopause flank regions (see Figure 4(e)). At such distances ($R > 7R_E$), E_ϕ 's integrated PSD values are dominated by “lower” (<4 mHz) frequencies, with this result being somewhat analogous to the SCA10 simulation results presented on the inset of Figure 4(a). As for the SA10 simulation, the presence of the driving frequency $f_o = 1.66$ mHz is clearly visible for the azimuthal (E_ϕ) PSD, but only at farther distances at the flanks, as presented in Figure 4(i).

Moving to the radial (E_r) component (Figures 2(e), (g), (h)), one can see that both the CIR and the Alfvénic fluctuations contributed to the RCA's IPSD in the flank regions of the modeled equatorial magnetosphere at larger radial distances, i.e., $\gtrsim 7R_E$. Intensification of the electric field radial component power at these local times and radial distances is most likely related to magnetopause boundary motions. For both synthetic simulations the magnetopause boundary is being pushed back and forth, but the cause for such a motion is quite different in each case. Whereas the SC simulation features essentially impulsive solar wind dynamic pressure variations as the main driver for ULF wave generation in the inner magnetosphere, the SA10 simulation, on the other hand, presents another mechanism for ULF wave generation, namely, purely Alfvénic fluctuations, which do not involve any noticeable density variations. In SA10 the rotation of the Alfvén wave's magnetic field in the y_{GSM} plane is the main contributor, since the field orientation on that plane changes from a mostly southward ($B_z < 0$) to a slightly northward ($B_z > 0$) orientation. Whenever the IMF has a southward component, the Region 1 Birkeland current strength is increased, and its associated magnetic field weakens the dayside magnetospheric field. As a result, the magnetopause moves inward to restore pressure balance with the solar wind flow (Sibeck et al. 1991). As the IMF subsequently changes to a northward orientation, however, the magnetopause retreats sunward, and thus the boundary motion will be driven by the IMF rotation in the imposed Alfvén wave.

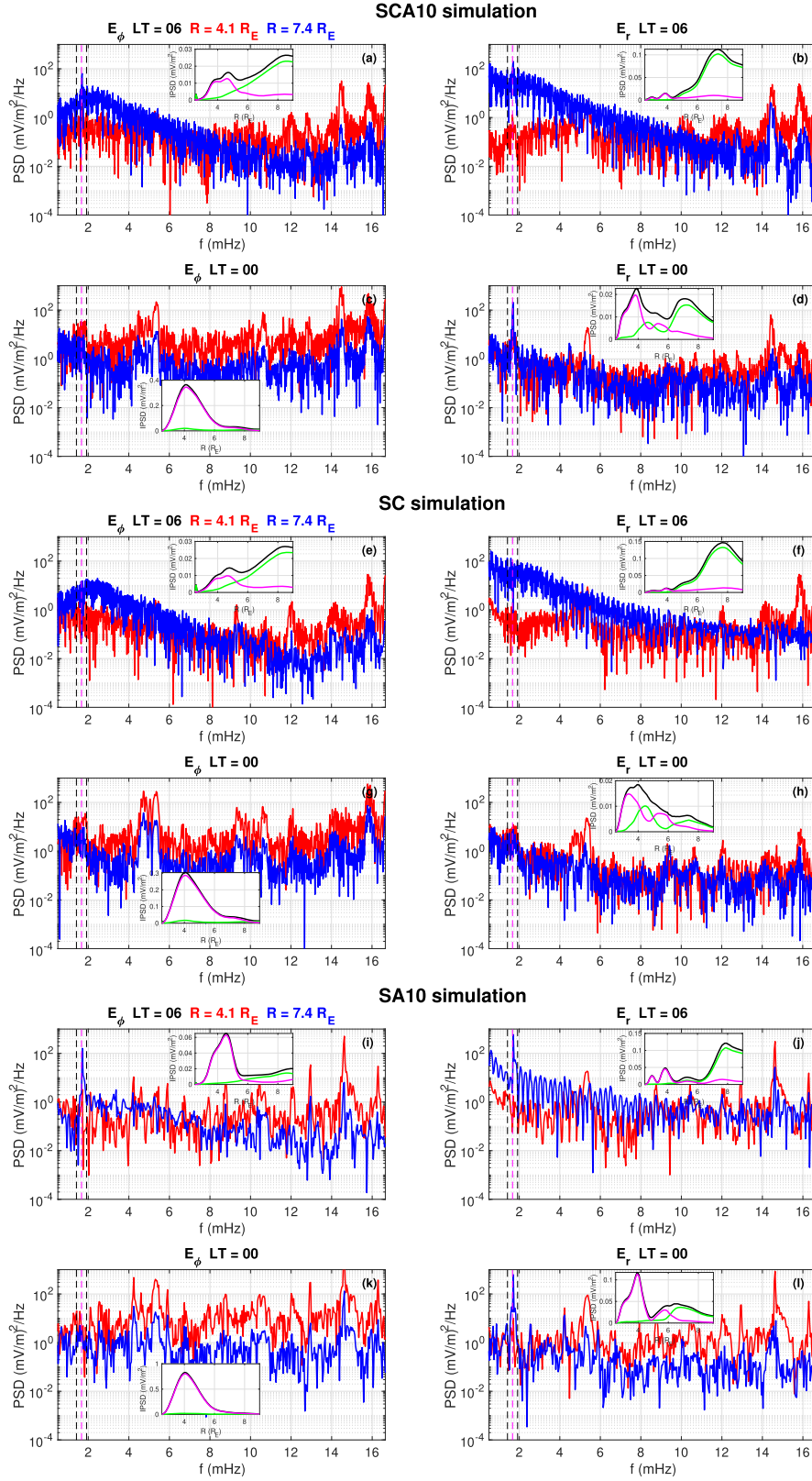


Figure 4. Fourier spectra of the azimuthal E_ϕ and radial E_r electric field components for the SCA10 (panels (a)–(d)), SC (panels (e)–(h)), and SA10 (panels (i)–(l)) simulations. Each Fourier spectrum is acquired at a given LT and radial distance R (in R_E , color-coded) as indicated on top of each panel. Insets show IPSD as a function of radial distance obtained along the indicated LT. Colored curves within the insets refer to PSDs integrated in three frequency bands, namely, $[0.5, 4]$ mHz (magenta), $(4, 16.66]$ mHz (green), and $[0.5, 16.66]$ mHz (black). Vertical black dashed lines indicate a narrow frequency band with 0.5 mHz width centered on the driving frequency $f_o = 1.66$ mHz (magenta dashed line).

At lower ($R < 4.1 R_E$) radial distances and specifically at local time sectors 04:00–06:00 LT and 20:00–00:00 LT, IPSD_r intensification seen in the RCA event’s simulation is captured by the other two synthetic simulations, i.e., SC and SA10, only when their corresponding Fourier spectra are integrated over the whole [0.5, 16.6] mHz band (see Figures 2(e), (g)). Figure 2(h) shows, instead, the PSD integrated only over a narrow band centered on the driving frequency for the SA10 simulation, that is, $f_o = 1.66$ mHz, and no IPSD_r intensification is seen in the aforementioned innermost region, which then tells us that the driving frequency does not seem to play a role for IPSD_r at such lower radial distances. The above-mentioned IPSD_r intensification is related to electric field fluctuations occurring at “higher” (>4 mHz) frequencies, as one can see in the insets of Figures 4(f), (h), (j), (l). These “higher” frequencies are present for all synthetic simulations (compare red lines in Figure 4). As already mentioned above, we have reasons to believe that such “higher” frequencies at lower radial distances are due to internal magnetosphere dynamics as modeled by the RCM model, as is briefly discussed in Section 5 below. Indeed, the Claudepierre et al. (2016) global MHD simulation results with the LFM code (Lyon et al. 2004) have shown that higher-frequency electric field fluctuations in both azimuthal and radial components penetrate deeper on the dayside inner magnetosphere whenever the RCM model is coupled to the LFM global MHD model. It is emphasized that Figure 3 of Claudepierre et al. (2016) clearly suggests that there is an enhancement on the integrated PSD, at least for the radial electric field component, also on the nightside magnetosphere for radial distances closer to Earth. It is true that Claudepierre et al. (2016) also included a plasmasphere model that increases appreciably (by 2 or 3 orders of magnitude) the particle number density nearer Earth. In our study, however, we did not include a plasmasphere model, but even so we obtained similar conclusions to those reported by Claudepierre et al. (2016).

Up to now, we have been comparing the integrated power spectral densities from the modeled RCA event with those from simulations featuring solar wind input parameters that have Alfvénic fluctuations with a period of 10 minutes ($f_o = 1.66$ mHz). It is known that actual solar wind fluctuations have a mixture of many frequencies; thus, we decided to also investigate the electric field component activity in the ULF frequency range when the magnetosphere is under the influence of solar wind Alfvénic fluctuations with a higher period, i.e., $T_f = 20$ minutes, which has been used elsewhere (e.g., Souza et al. 2017b). Figure 5 has the same format as Figure 2, with the only difference being panels (b) and (f) and panels (d) and (h), which show the $\text{IPSD}_{\phi,r}$ results for simulations SCA20 and SA20, respectively, with the corresponding PSDs being integrated in a narrow band centered on the driving frequency $f_o = 0.83$ mHz.

When using a higher fluctuation period, one can see that IPSD_r for the SCA20 simulation (Figure 5(f)) shows values along the flank regions that are (by a factor of ~ 2) higher than those for the SCA10 simulation (Figure 2(f)), and consequently closer to the reference IPSD_r values of the RCA event (Figure 2(e)). As with the IPSD_{ϕ} values for the SCA10 simulation, those for the SCA20 simulation did not show appreciable (or discernible) enhancements either in local time or in radial distance. A closer inspection of the E_{ϕ} ’s Fourier spectra for the SCA20 simulation at larger ($R \gtrsim 7 R_E$) radial distances (not shown) clearly reveals the presence of the

driving frequency with a power of about one order of magnitude higher than those at the neighboring frequencies. This result is similar to that of the SCA10 simulation, as presented in Figure 4(a). Such IPSD_{ϕ} enhancements at these farther-out locations are also most likely related to magnetopause boundary motions, since both the radial and azimuthal electric field components are expected to be excited near the magnetopause flanks whenever the magnetopause is pushed inward and outward, as presented on the sketch in Figure 9 in Appendix C. Also analogous to the SCA10 simulation results, IPSD_{ϕ} is dominated by the “higher” (>4 mHz) frequencies mentioned above for regions closer ($R \lesssim 4 R_E$) to Earth.

The pure Alfvénic fluctuation component with a 20-minute period (Figures 5(d), (h)) showed enhanced radial (E_r) electric field component activity essentially at the same local time sectors of those in the SA10 simulation, albeit with higher (by a factor of ~ 2) IPSD_r values. As for the azimuthal electric field component (SA20, Figure 5(d)), enhanced activity at the driving frequency ($f_o = 0.83$ mHz) was seen essentially at all local times as confirmed by inspection of E_{ϕ} ’s Fourier spectra (not shown) but only for radial distances larger than about $7 R_E$. At such farther-out distances, however, electric field fluctuations at the driving frequency are dominated by the radial component, which is characteristic of all synthetic simulations performed in this study, as one can see in Figures 3(b)–(f).

4.2. IPSD_s Using 2 hr Long Time Series

In order to better understand the behavior of the power generated by ULF waves in the nightside inner magnetosphere, we performed the integration of both E_{ϕ} ’s and E_r ’s Fourier spectrum into 2 hr long intervals. In this way, one can correlate IPSD changes with variations in solar wind parameters. It is emphasized that with a 2 hr long time series, which contains 240 data points, the frequency resolution used in the Fourier analysis is $\Delta f = 0.1389$ mHz. If the driving frequency one wishes to analyze is too “close” from the DC frequency component, the spectral power at the desired frequency might be impacted by the power at lower frequencies (due to intrinsic characteristics of the Fourier analysis itself), rendering the results ambiguous. For our study, however, this effect does not adversely impact our interpretations. In particular, for the SCA10 simulation the corresponding driving frequency is “farther” away from the DC component (about 12 times Δf) when compared to the driving frequency of the SCA20 simulation (about 6 times Δf), which is still far enough from the DC component. Using, however, shorter time series, i.e., having a lower number of data points with, say, half the number we are using here, could invalidate the usage of this “chunked” technique to analyze outputs from the SCA20 simulation, since the driving frequency in this case ($f_o = 0.83$ mHz) would be perilously close to the DC frequency component.

Figure 6 shows time sequences for both IPSD_{ϕ} and IPSD_r values for the SCA10 simulation. The top row in Figure 6 shows IPSD_{ϕ} values, whereas the bottom row shows IPSD_r values. The first and third 2 hr long intervals, going from 12:00 UT to 14:00 UT (panels (a) and (e)) and from 21:00 UT to 23:00 UT (panels (c) and (g)), encompass, respectively, the magnetosphere compression and decompression periods that occur when the solar wind density suddenly increases at around 13:00 UT and then decreases at around 22:30 UT on April 20—see Figure 1(a). We note that for these 2 hr long periods, and

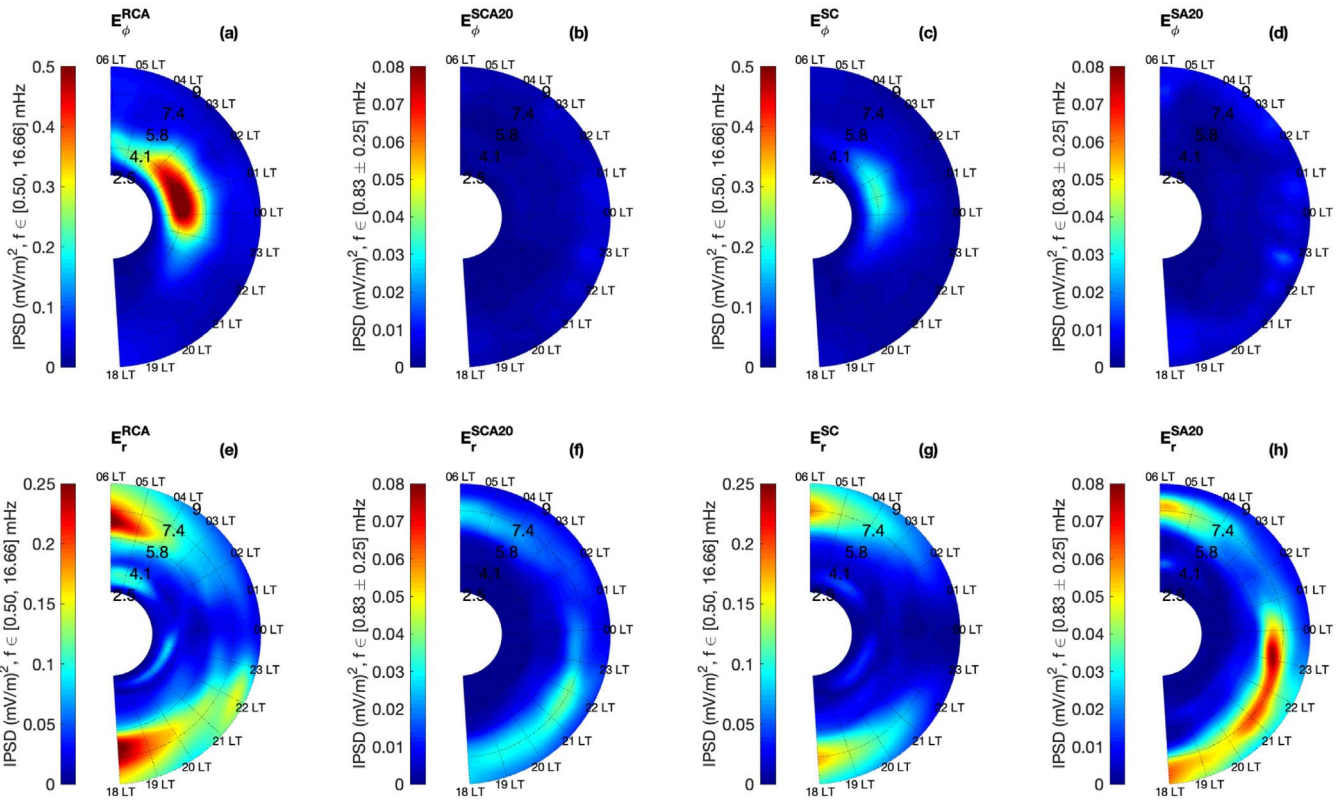


Figure 5. Same as Figure 2, but with input solar wind Alfvénic fluctuations having a period T_f of 20 minutes. The simulation identifiers that refer to such a period are SCA20 and SA20.

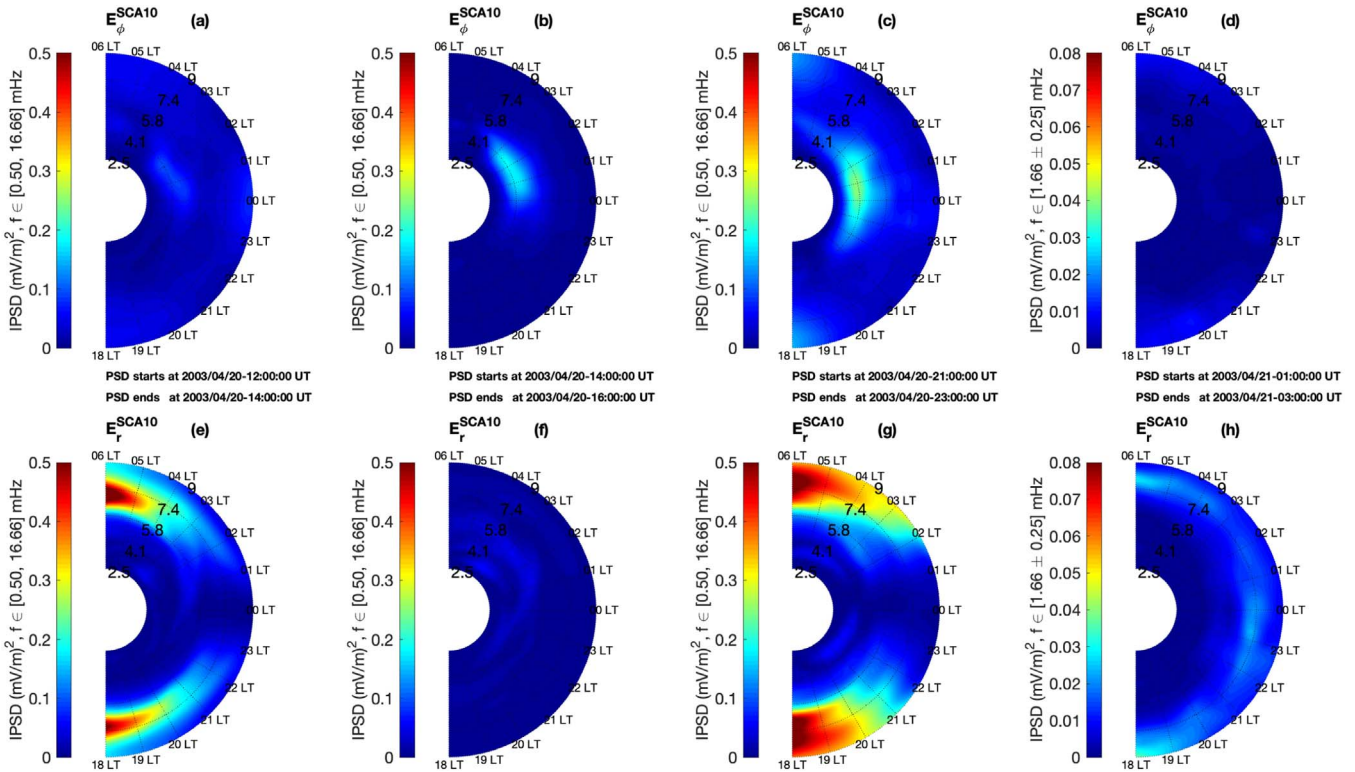


Figure 6. IPSDs of the E_ϕ (top row) and E_r (bottom row) components in the nightside, equatorial region of the terrestrial magnetosphere considering 2 hr long time periods that are indicated in between panels (a) and (e), panels (b) and (f), panels (c) and (g), and panels (d) and (h). The first (12:00–14:00 UT) and third (21:00 to 23:00 UT) 2 hr long periods encompass the abrupt variation in the solar wind density. During the second period, from 14:00 to 16:00 UT (panels (b) and (f)), there are no solar wind density variations, although Earth is subject to an intensified, yet constant, solar wind density. The fourth period, from 01:00 to 03:00 UT (panels (d) and (h)), captures part of the time wherein Earth is subject to synthetic solar wind Alfvénic fluctuations. Results are shown for the SCA10 simulation.

also for the other intermediate period shown in Figures 6(b), (f), the power spectral densities have been integrated considering the whole frequency band, i.e., from 0.5 to 16.66 mHz, since the magnetosphere is driven with a particular frequency only at 00:30 UT onward on April 21.

Comparing panels (e), (f), and (g) of Figure 6, one can see that particularly on the flanks (i.e., at 04:00–06:00 LT and 18:00–20:00 LT) of the modeled magnetosphere the radial electric field component responds strongly to magnetopause boundary motions driven by solar wind density (and therefore dynamic pressure) variations present during the CIR period as shown in Figure 1(a). When there are no solar wind density variations, however, which occurs, for instance, during the 2 hr long time period presented in panels (b) and (f), the IPSD_r values barely change. Indeed, at the flanks of the modeled magnetosphere the radial component in the FAC system is the most likely one to be excited owing to magnetopause boundary motions, as presented in the sketch in Figure 9 in Appendix C. Although difficult to see in panels (a), (b), and (c) of Figure 6, IPSD_ϕ slightly increases whenever solar wind dynamic-pressure-driven magnetopause boundary motions are present (panels (a) and (c)).

By comparing panels (a) and (c) of Figure 6, IPSD_ϕ values are more intensified for the latter case, despite the fact that both cases featured quite similar solar wind density variations of about 10 cm^{-3} . We draw the reader’s attention, though, to the fact that at 22:30 UT, thus within the 2 hr long period used for obtaining IPSD_ϕ in Figure 6(c), the IMF B_z component changed from a slightly positive, on average, $\sim 0.6 \text{ nT}$ value to a large negative $\sim -6 \text{ nT}$ value and remained so up to 00:30 UT. Therefore, for a period of less than 30 minutes (since the new solar wind information takes a few minutes to propagate from the global MHD input boundary at $x_{\text{GSM}} = 32 R_E$ to the modeled bowshock nose location at around $x_{\text{GSM}} = 15 R_E$, and from there the solar wind starts to effectively interact) the magnetosphere was under the influence of a large southward ($B_z < 0$) and also a relatively large ($\sim -5 \text{ nT}$) downward ($B_y < 0$) IMF. Hence, for a few tens of minutes magnetospheric convection was intensified and the magnetosphere was prone to substorm activity, which in turn has been previously argued (see, e.g., Southwood 1976; Cao et al. 2008; Liu et al. 2013, and references therein) to be one of the mechanisms explaining the generation of azimuthal electric field fluctuations on the nightside magnetosphere. Indeed, the Auroral Electrojet (AE) index data (see Figure 10 in Appendix D) evidenced substorm activity particularly after 22:00 UT, when AE reached peak values of about 1000 nT. We then suspect that the enhanced IPSD_ϕ activity shown in Figure 6(c), as well as in Figures 2(a), (c), might be related to magnetotail activity, particularly substorm injections, which in turn impacts the storm-time ring current buildup and therefore the plasma thermal pressure distribution on the nightside magnetosphere (see, e.g., Fok et al. 2003, and discussion in Section 5 of this paper). Moreover, such fluctuations are dominated in these regions by higher frequencies that do not involve the driving frequencies being analyzed in this study, so these fluctuations appear to be internally driven by the dynamics of the RCM (see, e.g., Toffoletto et al. 2003), as discussed in Section 5.

Lastly, the last 2 hr long time series “chunk” analyzed in Figures 6(d), (h), which features part of the Alfvénic fluctuation period, displays a quite similar behavior to that shown in Figures 2(b), (f), since in both cases the power spectral

densities are being integrated in a narrow band around the driving frequency $f_o = 1.66 \text{ mHz}$. Again, the radial component (Figure 6(f)) responded to the driving frequency oscillation mostly at larger radial distances and at nearly all local times, whereas the azimuthal electric field component, although having comparatively lower IPSD values, responded to the driving frequency as well but only at the flanks of the magnetosphere at larger ($\gtrsim 7R_E$) radial distances.

5. Discussions

The evaluation of the IPSDs in the equatorial, nightside magnetosphere allowed us to infer the relative importance of both azimuthal and radial electric field components during times when the magnetosphere is under the influence of a recurrent interplanetary structure, such as the RCA event analyzed here. A global MHD simulation of the 2003 April RCA event has shown that in the innermost regions of the modeled inner magnetosphere, i.e., at radial distances between $\sim 3R_E$ and $\sim 5.5R_E$ and in the 23:00–03:00 LT sector, fluctuations in the ULF frequency range of the azimuthal (E_ϕ) component were at least one order of magnitude higher than those of the radial (E_r) component, as shown in Figure 3(a). At farther-out distances, however, particularly in the flank regions, ULF frequency range fluctuations in the radial component were dominant, surpassing the IPSD values associated with the azimuthal component by a factor not larger than 8. In fact, such a predominance of the radial electric field component fluctuations in the flank regions was also seen for all other simulations performed in this study (see Figures 3(b)–(f)). Putting these results into the context of electron flux variability in the outer Van Allen radiation belt, one could conclude that either substorm injected or preexisting electrons would be subject, on their way to the dayside region, to elevated levels of ULF frequency range fluctuations of both electric field components, with each component playing a more important role on the electron–ULF wave interactions at different parts of the electron’s drift orbit (Claudepierre et al. 2008; Elkington 2006).

Separating the RCA event into its simpler constituent parts, namely, the CIR and solar wind Alfvénic fluctuations with a given fluctuation period, provided us with a way to understand the effects of each RCA component separately. For instance, regarding the intensified level of fluctuations in the E_ϕ component in the RCA event simulation (see Figure 2(a)), our global MHD simulation results with synthetic input parameters indicate that E_ϕ fluctuations nearer to Earth, i.e., at $R \lesssim 5.5 R_E$, are dominated by oscillations in the “higher” frequency band ($\geq 4 \text{ mHz}$) of the analyzed frequency domain $f \in [0.5, 16.66] \text{ mHz}$, as revealed by the IPSDs shown in the insets of Figure 4. Such internal E_ϕ fluctuations do not seem to be related to either of the two driving frequencies used in this study, as suggested by the results presented in panels (b) and (d) of Figures 2 and 5, which show the PSD integrated in a narrow band centered on either of the driving frequencies. On the other hand, at larger radial distances, that is, at $R \gtrsim 7 R_E$, and only along the flanks of the modeled magnetopause, azimuthal (E_ϕ) electric field fluctuations show a significant PSD peak at both driving frequencies, with this behavior being most likely due to magnetopause boundary motions driven solely by Alfvénic fluctuations, which in our numerical experiments do not involve any noticeable solar wind density (and therefore dynamic pressure) oscillations.

Since the aforementioned internal E_ϕ fluctuations do not appear to respond to either of the selected driving frequencies, we believe that the enhanced IPSD_ϕ values in Figures 2(a), (c) must be intimately related to internal magnetosphere dynamics as resolved by the RCM model (Fok et al. 2003; Toffoletto et al. 2003; De Zeeuw et al. 2004). The following line of reasoning provides a possible explanation for the spatial pattern of IPSD_ϕ values shown in panels (a) and (c) of Figure 2. Recall that the MHD electric field fluctuations shown here are obtained via $-\mathbf{V} \times \mathbf{B}$, so for our simulations the azimuthal electric field component is essentially given by $E_\phi \approx V_r B_\parallel$. The majority of the “higher” frequencies present in E_ϕ ’s time series are inherited from the bulk flow velocity component time series (not shown) rather than the magnetic field component; thus, understanding how the bulk flow behaves is the key to comprehending the spatial patterns in the IPSD_ϕ values shown in Figures 2(a), (c). Within the domain of the RCM model, which extends up to about $7R_E$ – $8R_E$ in geocentric distance, the bulk flow velocity is highly influenced by the RCM model, which provides a self-consistent description of the electro-dynamics of the coupled inner magnetosphere–ionosphere system (see De Zeeuw et al. 2004, for an in-depth view of the RCM coupling with the global magnetosphere module of BATS-R-US). The key point here is that RCM calculates a more accurate inner magnetosphere thermal plasma pressure by including transport of inner plasma sheet and ring current particles via gradient/curvature drifts. Such plasma pressure is mapped back to the global magnetosphere module of BATS-R-US. These corrected pressure values will have a direct impact on the MHD bulk flow velocity patterns via the numerical solution of both momentum and energy equations (see Equation (1) in De Zeeuw et al. 2004).

Our results in Figures 2(a), (c) show that IPSD_ϕ values nearer to Earth present a local time asymmetry with higher integrated ULF power concentrated in the dawn–midnight sector. A modest dawn–dusk asymmetry in RCM’s thermal pressure distribution has also been reported previously (see Figure 2 in De Zeeuw et al. 2004, for details). We argue that the local time asymmetry seen in our simulation results for the internal IPSD_ϕ values is being influenced by the thermal pressure distribution as set up by the RCM model. To the best of our knowledge, however, the cause for such modest dawn–dusk asymmetry has not been conclusively established, but some plausible explanations have been invoked, such as the effect of ionospheric conductance gradients on the location of the ring current peak, and therefore the location of the thermal plasma pressure peak (see, e.g., Section 4 of Fok et al. 2003, for further details). We also point out that enhanced magnetospheric convection and substorm injections might be playing a role in the thermal pressure distribution on the nightside magnetosphere (see, e.g., Fok et al. 2003). More investigations on this matter might be worth pursuing, but we leave those for future studies.

When trying to understand the ULF frequency range fluctuations in the E_r component in the flank regions, the results from our numerical experiments suggest that both the CIR and the monochromatic solar wind Alfvénic fluctuations played important roles, since the E_r component is expected to be more excited along the flanks (Claudepierre et al. 2008; Elkington 2006) owing to magnetopause boundary motions (see Figure 9 in Appendix C). As mentioned in Section 4.1, the causes for the magnetopause to be pushed inward and outward

during a CIR and during solar wind Alfvénic fluctuations are quite different, since in the former the magnetopause is moved owing to abrupt changes in the solar wind dynamic pressure, whereas in the latter the magnetopause boundary motion is driven solely by the rotation, on the yz_{GSM} plane, of the wave’s magnetic field.

Lastly, it is emphasized that IPSD amplitudes in the SC simulation underestimated those of the RCA event simulation, as one can see when comparing panels (a) and (c) and panels (e) and (g) of Figure 2. This result is not so surprising since we are simplifying the solar wind input data considerably. Consider, for instance, the real solar wind density variations in Figure 1(a). One will notice that it increases about 35% prior to the sudden decrease at around 22:30 UT. By virtue of what has been shown in Section 4.2, this increase in density will lead to further magnetosphere compression, therefore increasing the fluctuations in both electric field components, particularly in the E_r component. The synthetic solar wind input does not take such an effect into account, since the parameters are held constant during some intervals. The advantage of constructing the synthetic inputs, though, by taking averages of the real data is that one can get rid of further complexities in the original signal, which fluctuates appreciably, and can focus only on the parameter’s baseline changes.

6. Summary and Conclusions

In this work a numerical study was carried out to understand the contributions to the convection electric field fluctuations in the ULF frequency range when Earth’s magnetosphere was under the influence of an interplanetary structure composed of a CIR followed by solar wind Alfvénic fluctuations. This type of solar wind structure, referred to as “RCA,” has been chosen in our study since it can occur in any phase of the solar cycle, but it is more often observed during the declining phase. Moreover, such structures are known to promote a series of disturbances in the inner magnetosphere, including the excitation of ULF waves.

We employed a series of controlled numerical experiments whereby a simplified set of solar wind parameters were provided as input to the global MHD SWMF/BATS-R-US model, which was coupled to an inner magnetosphere model (Toffoletto et al. 2003) and to an ionospheric electrodynamics model (Ridley et al. 2004). Specifically, a total of six global MHD simulations were performed, as listed in Table 1. The first of these simulations used actual solar wind input parameters from the RCA event on 2003 April. The other five simulations featured synthetic solar wind input profiles that were built using appropriate time averages of the real solar wind parameters, as indicated in Table 2. The idea behind these simplified numerical experiments was to understand the role of each RCA’s component on the electric field fluctuations in the [0.5, 16.66] mHz ULF frequency range.

The main findings of this study can be summarized as follows:

1. The modeled RCA event, which had its corresponding power spectral densities integrated in the whole analyzed frequency domain, that is, from 0.5 to 16.66 mHz, showed that azimuthal (E_ϕ) and radial (E_r) electric field component fluctuations were excited in different local time sectors and radial distances, with the azimuthal ones showing higher integrated power in the innermost region ($R \lesssim 5.5 R_E$) of the analyzed domain, and the fluctuations

associated with the radial component being predominant along the flanks of the modeled magnetosphere at larger radial distances ($R \gtrsim 7 R_E$), with the latter result being in accordance with previous works (Claudepierre et al. 2008, 2010; Elkington 2006).

2. Both SCA10 and SCA20 simulations, whose input solar wind parameters resembled the observed RCA event, had their corresponding power spectral densities integrated in narrow bands centered on the respective driving frequencies. For both numerical experiments, we found that the radial electric field component fluctuations showed enhanced spectral power at the respective driving frequencies, particularly at the flanks of the magnetopause, but only for larger radial distances, i.e., $R \gtrsim 7 R_E$. At such locations, the radial component is expected to be excited owing to magnetopause boundary motions, which are driven in our simulations either by solar wind dynamic pressure pulses, which are characteristic of CIRs, or by pure Alfvénic fluctuations. As for the azimuthal electric field component, we showed that fluctuations closer to Earth, that is, $R \lesssim 5.5 R_E$, are dominated by frequencies larger than both driving frequencies studied in this work. Thus, such innermost azimuthal oscillations do not appear to directly respond to any of the two kinds of upstream Alfvénic fluctuations. E_ϕ 's Fourier spectra at the outermost ($R \gtrsim 7 R_E$) locations, however, do show a peak in the PSD at both driving frequencies, mostly at the flanks of the magnetopause, although the corresponding integrated power spectral densities are lower than those for the radial electric field component at the same locations.
3. By performing the Fourier spectrum integration on 2 hr long intervals, we are able to correlate changes in the IPSD values to variations in the solar wind parameters. When comparing panels (a) and (c) of Figure 6, wherein the power spectral densities are integrated in the whole analyzed frequency domain, the innermost ($R \lesssim 5.5 R_E$) IPSD $_\phi$ values are intensified when inner magnetosphere plasma convection is enhanced owing to a southward turning of the IMF B_z (see detailed explanation in Section 4.2). Such IPSD $_\phi$ intensification occurred before the beginning of the Alfvénic fluctuations, which suggests that such internal azimuthal electric field oscillations and solar wind Alfvénic fluctuations with a particular driving frequency are apparently unrelated. Moreover, the radial electric field component responded to periods of both abrupt solar wind density variations and solar wind Alfvénic fluctuations.

P.R.J. thanks the financial support from the China-Brazil Joint Laboratory for Space Weather for his Postdoctoral fellowship. This work was carried out using the SWMF/BATSRUS tools developed at the University of Michigan Center for Space Environment Modeling (CSEM) and made available through the NASA Community Coordinated Modeling Center (CCMC). Data at the L1 Lagrangian point provided by the ACE spacecraft can be readily found at <http://www.srl.caltech.edu/ACE/ASC/level2/index.html>. V.M.S. thanks the São Paulo Research Foundation (FAPESP) grant 2014/21229-9 and the Brazilian National Council for Scientific and Technological Development (CNPq) PCI grant 301228/2019 for support. M.V.A. thanks CNPq/MCTIC (310900/2016-6),

and E.E. thanks the CNPq/PQ-302583/2015-7 and FAPESP (2018/21657-1). The authors thank MCTIC/FINEP (CT-INFRA grant 0112052700) and the EMBRACE Space Weather Program for the computing facilities at INPE. The authors also acknowledge the invaluable comments and suggestions put forth by the anonymous referee.

Appendix A Ground Magnetometer Data

We made use of geomagnetic field measurements from ground-based magnetometer stations to check ULF wave activity in the inner magnetosphere during the period of interest. The analyzed temporal and spatial distribution of the ULF wave power was in the 1–8.33 mHz frequency range. The time series obtained from ground-based station arrays were provided by the SuperMag collaboration (Gjerloev 2009). Most of these stations are part of the International Monitor for Auroral Geomagnetic Effect network (Tanskanen 2009). The chosen stations are located close to the Corrected Geomagnetic (CGM) longitude of 110° and have a latitudinal coverage that goes from around 36° up to 67.3° , which corresponds to McIlwain L parameter (McIlwain 1961), or L shell, with values in the $1.5R_E$ – $6.75R_E$ range ($R_E =$ Earth radius). Table 3 shows the station code and the corresponding CGM coordinates and L shell for the 22 stations used in this work. The measured geomagnetic field has a 1-minute time resolution, which is enough to obtain ULF waves in the Pc4–5 frequency range (Jacobs et al. 1964). The signal was filtered using a bandpass Butterworth filter with cutoff frequencies between 1 and 8.33 mHz. In order to analyze the signal in the frequency domain, a continuous wavelet transform with a Morlet mother function has been applied to the filtered data to generate the wavelet power spectrum density (WPSD). The mean frequency power was extracted from the WPSD to obtain the quantitative

Table 3
Locations of 22 Ground-based Magnetometer Stations in the Corrected Geomagnetic Coordinates

Station	CGM Long. (deg)	CGM Lat. (deg)	L Shell (R_E)
SOR	106.21	67.30	6.75
TRO	102.95	66.68	6.35
KEV	109.27	66.28	6.21
KIL	130.85	65.78	5.98
ABK	101.82	65.18	5.72
IVA	108.61	65.03	5.65
MUO	105.26	64.61	5.47
KIR	102.69	64.56	5.46
SOD	107.29	63.81	5.18
PEL	104.95	63.42	5.05
OUJ	106.15	60.82	4.25
HAN	104.63	58.51	3.71
NUR	102.2	56.70	3.35
LOV	96.06	55.74	3.18
TAR	102.92	54.33	2.96
HLP	95.19	50.79	2.50
BEL	96.09	47.84	2.21
LVV	98.22	45.76	2.04
HRB	92.81	43.58	1.88
THY	92.02	42.49	1.82
SUA	99.57	40.48	1.73
ISK	101.58	35.95	1.51

Note. The dipole L shell parameter for each station is also shown.

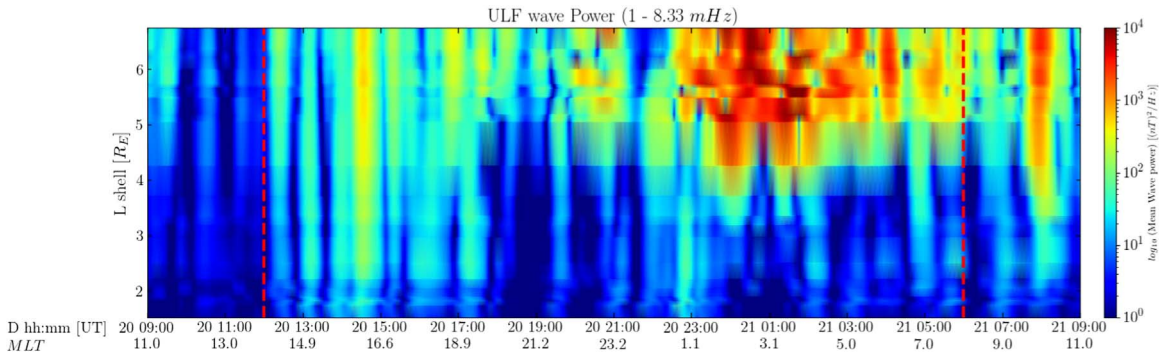


Figure 7. Mean Pc5 wave power for the ground-based horizontal magnetic field component for 22 stations nearly aligned at 110° CGM longitude and spanning about 30° in CGM latitude, as shown in Table 3. The period of analysis was 24 hr starting on April 20 at 09:00 UT. The vertical axis represents the L shell values plotted against the time in UT and MLT. The color shows the mean ULF power between 1 and 8.33 mHz. The red dashed lines encompass an 18 hr long period that will be further analyzed using global MHD simulations.

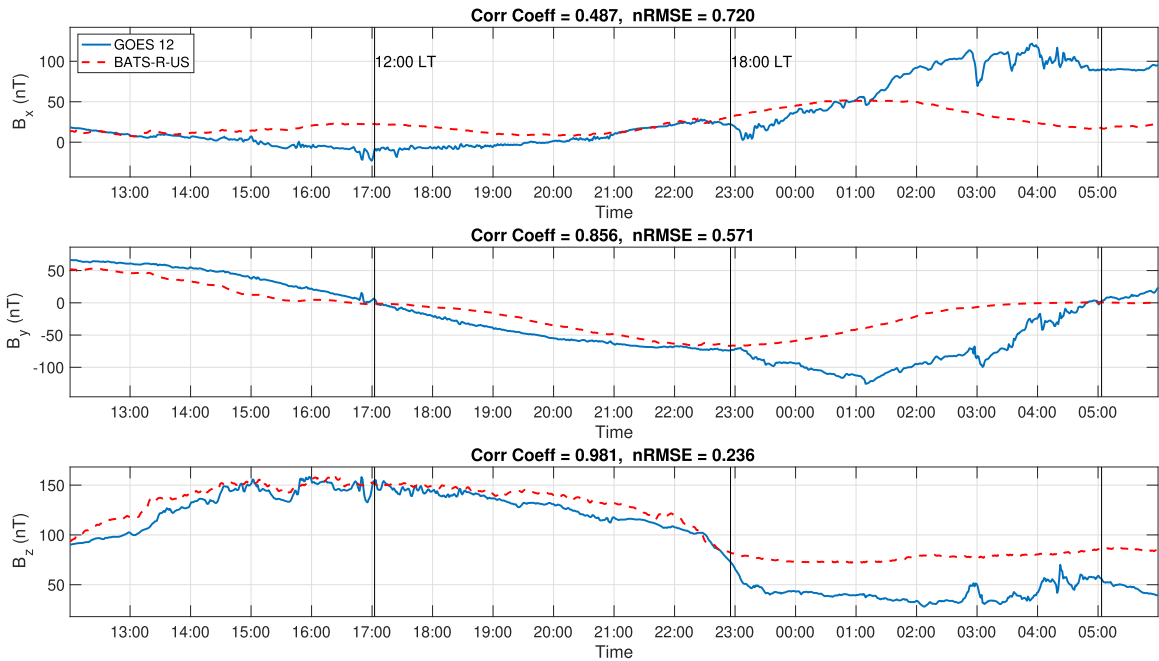


Figure 8. Comparison between *GOES-12*'s (blue line) magnetic field components and *BATS-R-US*'s (red dashed line) magnetic field components obtained along *GOES-12*'s orbit, using the RCA event simulation outputs, during an 18 hr long period starting at 12:00 UT on 2003 April 20. The linear correlation coefficient and nRMSE values, as done by Welling & Ridley (2010), are shown on top of each panel.

information about the waves for each station with respect to the CGM latitude and L -shell value, as presented in Figure 7.

error (nRMSE) as calculated by Welling & Ridley (2010). Both correlation coefficient and nRMSE values are shown on top of each panel.

Appendix B MHD Simulation Output Data Taken along *GOES-12* Orbit

Figure 8 shows the magnetic field outputs from the RCA simulation (red dashed line) taken along *GOES-12*'s orbit path during an 18 hr long period starting at 12:00 UT on April 20. *GOES-12* magnetic field data are shown as blue lines for comparison with RCA simulation data. The level of agreement between observational and modeled data is assessed via the correlation coefficient and the normalized root-mean-squared

Appendix C Magnetopause Boundary Motions

Considering the configuration of the FAC system ($b_{||}$, r , ϕ) at the flanks of the magnetopause, as shown in the sketch presented in Figure 9, magnetopause boundary motions driven either by solar wind dynamic pressure variations or by solar wind magnetic field oscillations of Alfvénic nature are expected to excite electric field variations at these locations

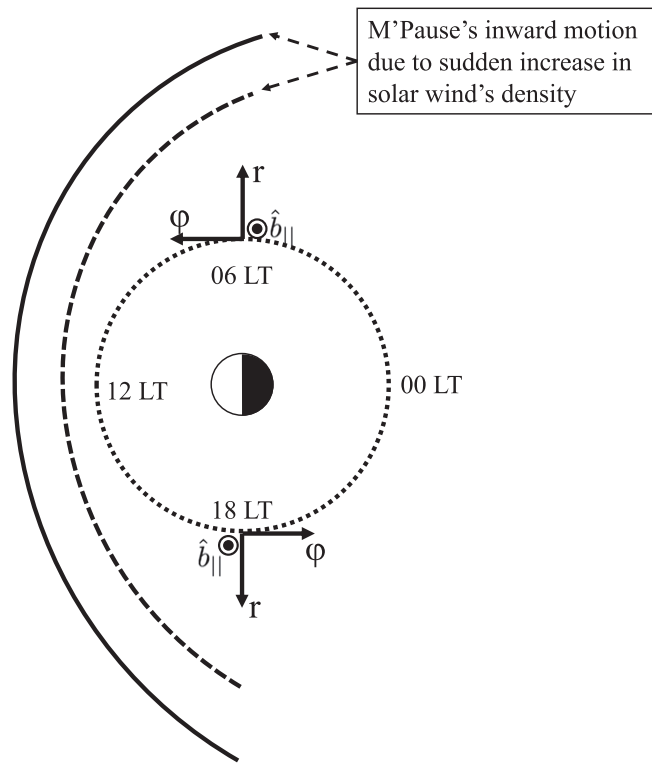


Figure 9. Sketch of field-aligned coordinate system (b_{\parallel} , r , ϕ) at the equatorial magnetosphere. The magnetopause position is depicted for two instances, namely, before (solid line) and after (dashed line) the magnetosphere’s compression owing to a sudden increase in the solar wind density.

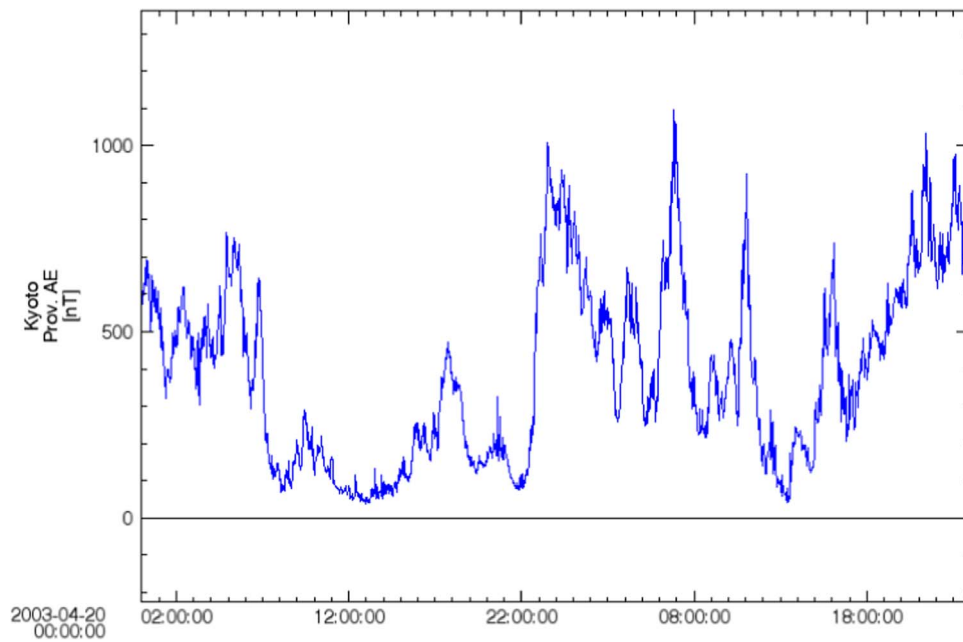


Figure 10. Two days of AE index data starting on 2003 April 20 at 00:00 UT. The interval analyzed on the manuscript goes from 12:00 UT on April 20 up to 06:00 UT on April 21. Substorm activity picks up around 22:00 UT onward.

mostly along the radial direction, which addresses the lower $IPSD_{\phi}/IPSD_r$ ratios in Figure 3.

values indicative of substorm activity are present mostly at 22:00 UT onward, when the IMF B_z reaches its highest negative value (~ -6 nT).

Appendix D Auroral Activity Index

Figure 10 shows the auroral electrojet (AE) index activity encompassing the analyzed period. Higher ($\gtrsim 800$ nT) AE

ORCID iDs

P. R. Jauer <https://orcid.org/0000-0002-8064-5030>
V. M. Souza <https://orcid.org/0000-0001-7294-7963>

H. Li  <https://orcid.org/0000-0002-4839-4614>
 C. Medeiros  <https://orcid.org/0000-0002-6914-5799>

References

- Alves, L. R., Souza, V. M., Jauer, P. R., et al. 2017, *SoPh*, **292**, 92
 Baker, D. N., Li, X., Turner, N., et al. 1997, *JGR*, **102**, 14141
 Cao, J., Duan, J., Du, A., et al. 2008, *JGRA*, **113**, A07S15
 Claudepierre, S. G., Elkington, S. R., & Wiltberger, M. 2008, *JGRA*, **113**, A05218
 Claudepierre, S. G., Hudson, M. K., Lotko, W., Lyon, J. G., & Denton, R. E. 2010, *JGRA*, **115**, A11202
 Claudepierre, S. G., Toffoletto, F. R., & Wiltberger, M. 2016, *JGRA*, **121**, 227
 Da Silva, L. A., Sibeck, D., Alves, L. R., et al. 2019, *JGRA*, **124**, 1660
 De Zeeuw, D. L., Sazykin, S., Wolf, R. A., et al. 2004, *JGRA*, **109**, A12219
 Dungey, J. W. 1961, *PhRvL*, **6**, 47
 Elkington, S. R. 2006, *GMS*, **169**, 177
 Ellington, S. M., Moldwin, M. B., & Liemohn, M. W. 2016, *JGRA*, **121**, 2033
 Fok, M.-C., Moore, T. E., Wilson, G. R., et al. 2003, *SSRv*, **109**, 77
 Gjerloev, J. W. 2009, *EOSTr*, **90**, 230
 Gombosi, T. I., DeZeeuw, D. L., Groth, C. P. T., et al. 2001, *GMS*, **125**, 169
 Jacobs, J. A., Kato, Y., Matsushita, S., & Troitskaya, V. A. 1964, *JGR*, **69**, 180
 Komar, C. M., Glocer, A., Hartinger, M. D., et al. 2017, *JGRA*, **122**, 12006
 Liu, W., Cao, J. B., Li, X., et al. 2013, *JGRA*, **118**, 4298
 Lyon, J., Fedder, J., & Mobarry, C. 2004, *JASTP*, **66**, 1333
 McGregor, S. L., Hudson, M. K., & Hughes, W. J. 2014, *JGRA*, **119**, 8801
 McIlwain, C. E. 1961, *JGR*, **66**, 3681
 Ogino, T., Walker, R. J., & Ashour-Abdalla, M. 1992, *ITPS*, **20**, 817
 Ozeke, L. G., Mann, I. R., Murphy, K. R., Jonathan Rae, I., & Milling, D. K. 2014, *JGRA*, **119**, 1587
 Powell, K. G., Roe, P. L., Linde, T. J., Gombosi, T. I., & Zeeuw, D. L. D. 1999, *JCoPh*, **154**, 284
 Prestes, A., Klausner, V., & Ojeda-González, A. 2017, *AnGeo*, **35**, 1231
 Ridley, A. J., Gombosi, T. I., & DeZeeuw, D. L. 2004, *AnGeo*, **22**, 567
 Sibeck, D. G., Lopez, R. E., & Roelof, E. C. 1991, *JGRA*, **96**, 5489
 Southwood, D. J. 1976, *JGR*, **81**, 3340
 Souza, V. M., Gonzalez, W. D., Sibeck, D. G., et al. 2017a, *JGRA*, **122**, 4228
 Souza, V. M., Lopez, R. E., Jauer, P. R., et al. 2017b, *JGRA*, **122**, 10,084
 Stone, E., Frandsen, A., Mewaldt, R., et al. 1998, *SSRv*, **86**, 1
 Takahashi, K., & Anderson, B. J. 1992, *JGRA*, **97**, 10751
 Tanskanen, E. I. 2009, *JGRA*, **114**, A05204
 Toffoletto, F., Sazykin, S., Spiro, R., & Wolf, R. 2003, *SSRv*, **107**, 175
 Tóth, G., van der Holst, B., Sokolov, I. V., et al. 2012, *JCoPh*, **231**, 870
 Tsurutani, B. T., Gonzalez, W. D., Gonzalez, A. L. C., et al. 2006, *JGRA*, **111**, A07S01
 Vasyliunas, V. M. 1975, *RvGeo*, **13**, 303
 Wang, C., Guo, X., Peng, Z., et al. 2013, *ScChE*, **56**, 1141
 Welling, D. T., & Ridley, A. J. 2010, *SpWea*, **8**, 03002